

A facile approach for fabrication of underwater superoleophobic alloy

Xiaolei Ma · Hao Luo · Jun Ma · Pengwei Wang ·
Xinlong Xu · Guangyin Jing

Received: 1 November 2012 / Accepted: 8 April 2013 / Published online: 24 April 2013
© Springer-Verlag Berlin Heidelberg 2013

Abstract Superoleophobicity developed by creating roughness at multiple scales or lowering the surface energy has drawn extensive attention for technological applications. Currently, most methods for fabrication of superoleophobic surfaces employ either the complicated manufacture of micro/nano structures or delicate chemical decorations. Here, the sharp wetting transition from an oleophilic state to an oleophobic one has been practically realized, and the mechanism successfully interpreted. The underwater superoleophobic surfaces are newly realized and successfully controlled by subtly tuning the surface morphology of the alloy by practical corrosion plus a naturally obtained, stable, high-energy inorganic coating layer which induces the sharp wetting transition from oleophilic state to oleophobic state. The contact angle (CA) variations are quantitatively analyzed based on the wetting model by employing a roughness geometrical structure and a corrosion mechanism, which agree well with the measured results. Additionally, the dependence of the roughness on the corrosion procedure is modeled microscopically. Our method uncovers a facile fabrication protocol for optimum underwater superoleophobic surfaces by modifying the microstructures of

alloy surfaces in the manufacturing process, which furthermore offers significant insights into the design and creation of other novel antifouling materials.

1 Introduction

Natural wetting phenomena have recently gained extensive attention in aspects of both theoretical formulation [1–3] and practical mimicry [4]. One such famous example is the lotus effect, which has aroused great interest because of its potential versatile applications in, e.g., self-cleaning [5], non-stick coatings [6], microflow regulation [7], fluid drag reduction [8], and so on. “Super-wetting” properties of a specific surface including superhydrophobicity, superhydrophilicity, and superoleophobicity are always of vital significance for their uses in industry and our daily life. Based on the classical models developed early by Wenzel [9] and Cassie and Baxter [10], various geometrical structures and chemical modifications have been widely employed to modulate the surface wettability for water and oil [11, 12].

A patterned surface with periodic micro/nano structures is commonly used in studies to vary the wettability [13, 14], where high-cost lithography or nanofabrication facilities are necessary. Also, chemical coatings with functional polymer film deposition are devoted to the modification of the wetting properties [15]. Additionally, combinations of nanostructured surfaces and further chemical coatings have also been developed to obtain desirable wetting characteristics, such as ZnO nanowire arrays covered with hydrophobic polymer layers [16], carbon nanotubes with polytetrafluoroethylene (PTFE) [17], and TiO₂ nanotube arrays on a micro-Ti structure via an electrochemical method with fluoroalkyl silanes [18]. A silicon-based water-repellent surface

X. Ma · H. Luo · J. Ma · X. Xu · G. Jing (✉)
Department of Physics & NanoBiophotonics Center, National Key Laboratory and Incubation Base of Photoelectric Technology and Functional Materials, Northwest University, Xi’an 710069, China
e-mail: jing@nwu.edu.cn
Fax: +86-29-88302115

P. Wang
Northwest Institute for Nonferrous Metal Research,
Xi’an 710016, China

X. Xu
Institute of Photonics and Photon-Technology, Northwest University, Xi’an 710069, China

with hierarchical morphology of two length-scale roughnesses was realized by utilizing ultra-fast (femtosecond) laser irradiation under a chemically reactive gas atmosphere of SF₆, as reported by Vassilia Zorba et al. [19]. Also, Eun Kyu Her et al. obtained superhydrophobic surfaces on alloyed steels with different Cr content using a method of plasma etching and subsequent water immersion treatment, which rendered the formation of high aspect ratio nanostructures, such as flakes or needles leading to superhydrophobicity [20].

In contrast, the fabrication of superoleophobic surfaces can be rather complicated. However, they have great potential applications as antifouling materials for use with hazardous chemicals and biological contaminants. Thus they have drawn increasing attention in the scientific community in the last decade following the observations of the microtextures of plant surfaces and the first development of super-water-repellent artificial surfaces possessing a fractal microstructure. So far, most of the reported artificially fabricated superoleophobic surfaces are only applicable in air; research on underwater water/oil-repelling surfaces is still limited to the best of our knowledge. Choi et al. developed a process of simple dip-coating of extremely low-surface-energy molecules and controllable geometry of the surface to tune the oleophobicity of fabrics [21]. Also, a novel geometry of the surface called the “re-entrant texture” was developed to modify the wettability for even low energy liquids such as methanol, octane, and pentane [11]. As a result, a contact angle (CA) of more than 150° on the peculiar geometrical and perfluorinated patterned surfaces was then obtained, whose physical mechanism was discussed later [22]. Moreover, Zhang et al. [23] prepared a superoleophobic surface consisting of CF₃-terminated oxidized-silicone nanofilaments with topographical features similar to the “perfectly hydrophobic surface” reported by Gao and McCarthy [24]. In addition to the fabrication of topographically modified surfaces to achieve superoleophobicity, there are some reports focusing on controlling the molecular configuration (e.g., branched, star-shaped molecules) and the physical nature of the modified surface to realize oleophobicity and desirable dewetting properties [25]. L. Jiang and colleagues recently found a novel method consisting of rough nanostructured hydrogel coatings and microscale porous metal substrates to produce both superhydrophilic and underwater superoleophobic materials [26]. Furthermore, biomimetic oleophobic or superoleophobic solid surfaces have also been achieved by emulating the functions of unique tissues in organisms [27, 28].

However, on one hand, the time-consuming or high-cost techniques for producing an artificial textured surface make it necessary to find more practical protocols and manufacturing techniques for manufacturing water/oil-repelling surfaces on a large scale. Chemical coatings suffer a practical limitation caused by robust adhesion problems on the

other hand. Motivated by the challenge of making a superoleophobic surface, here, by tuning the surface morphology via easily controllable corrosion accompanied by a naturally formed stable inorganic high-energy coating layer which induces a sharp wetting transition from oleophilic state to oleophobic state, a new facile procedure is proposed to realize the oil/water-repelling features. It is designed to systematically investigate the connection between the surface landscape and the wetting properties, which is in particular the correlation between the surface roughness and superoleophobicity, basing on the corrosion mechanisms and classical wetting models, which is of urgent requirement in industrial aspects of the oil-transmission process (especially for the controllable oil/water separation), bioadhesion, green constructions, and microfluidic systems [29–31].

2 Experiments and materials

2.1 Materials and solution

The alloy substrates from the pipeline industry with a dimension of 2.0 cm × 3.0 cm are cut from a sheet of API X100 pipeline alloy. The chemical composition is shown in Table 1.

To modify the surface roughness of the alloy substrates, these alloy samples are polished with different levels of silicon carbide (SiC) sheets (80, 150, 400, 600, 1000, 1500, 2000 grit) and 1.5 μm diamond paste. Finally, four categories of the samples are prepared: (1) bare sample (used as received, no polishing); (2) preliminarily polished sample (polished with 80, 150, and 400 grit sheets in sequence); (3) further polished sample (polished with 600, 1000, and 1500 grit sheets in sequence); (4) finely polished sample (polished with 1500, 2000 grit sheets and diamond paste in sequence). After polishing, each polished sample exhibits a different level of roughness, which is defined here as the initial roughness for each one. Thereafter, all the samples are corroded with 10 wt.% HCl solution (AR grade, Beijing Chemical Engineering Co. Ltd.) at room temperature for different times, respectively, and are finally kept in boiled deionized water (Di-water) for further use.

2.2 Corrosion process and contact angle measurement

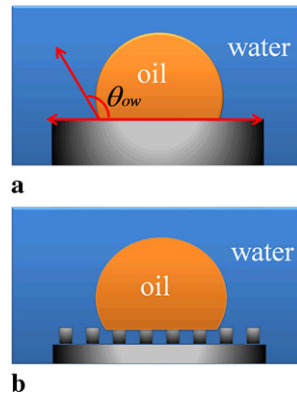
Five groups (four pieces/group) of substrates are defined by corrosion in identical HCl solutions for different times (0, 0.5, 2, 5, 9 h). Before the corrosion processes, these samples are cleaned first with acetone, then with alcohol in an ultrasonic pool two times, and then with Di-water, which can reduce contamination by organic adsorption and dust. In order to evaluate the effect of polishing on the wettability of the alloy substrates for oil, the CA measurement for a sessile oil (1,2-dichloroethane) drop (see the sketch in Fig. 1)

Table 1 Chemical composition of X100 pipeline alloy substrates (weight fractions, %)

C	Si	Mn	Cu	Al	Nb	Ti	Ni	Mo	S	P	Fe
0.064	0.13	1.56	0.38	0.030	0.089	0.001	0.54	0.28	0.0024	0.024	Balance

Fig. 1 Sketch of the oil drop resting on the alloy substrate surrounded by water.

(a) Diagram of an oil droplet lying on a smooth substrate with a CA θ_{ow} , and (b) on a rough substrate



is performed for each substrate under water at room temperature (~ 25 °C). By using a microsyringe, the oil droplet (about 4–9 μL in volume) is gently deposited on each substrate perpendicularly. The image of the sessile oil drop is captured from the side view by the camera system (CCD F201-B+Nikkor 60 mm/2.8 lens) and then analyzed by ImageJ software for CA measurement. We note that after corrosion the substrates are all cleaned by alcohol in the ultrasonic pool and Di-water five times to remove the HCl residues before the CA measurements in order to eliminate the effect of chloride ion on the CA of the oil droplet. The surface roughness measurements are performed with a tapping-mode atomic force microscope system (AFM, Dimension icon, Bruker Co. Ltd.); additionally, a scanning electron microscope (SEM, JSM6390A, Japan) and X-ray photoelectron spectroscopy (XPS, WSCALAB, 205x1) were employed to obtain the overall surface morphology and chemical nature of the corroded samples. The X-ray diffraction (XRD) patterns are collected on a D/MAX-3C system using graphite-monochromatized Cu K α radiation ($\lambda = 1.5406$ Å) for all the examined samples.

3 Results

3.1 Surface roughness after polishing

To evaluate the surface roughness of the substrates after polishing, atomic force microscopy (AFM) measurements are conducted for the samples after the different polishing processes (Fig. 2). The root mean square (RMS) roughness decreases significantly from 21.21 nm for the bare sample (Fig. 2a) to 0.17 nm for the finely polished sample (Fig. 2d). As the polishing for the substrate surface in present work

is conducted along one direction, the texture of directional trenches (or grooves) is easily seen in the AFM images.

3.2 Contact angle measurement

The water partially wets the finely polished substrate surface in air with a CA of 72°, as Fig. 3a shows (the reported CA is the mean value of different measurements and the standard deviation denoted here within 0.13 % for all CA measurements in this report), in contrast, the oil droplets almost totally spread (CA < 5°, Fig. 3b) on this substrate, which is due to the lower surface tension of the oil in the ambient condition. The CA measurements for the oil drop in water are displayed in Fig. 3c and 3d. Clearly, the oil drop cannot spread on the alloy substrates surrounded by water. The CA is 122° (Fig. 3d) on the bare sample, and is 85° (Fig. 3c) on the finely polished one, which suggests that the wettability of samples for oil is strongly dependent on the roughness of substrates' surfaces.

As shown in Fig. 4, samples corroded for different times exhibit distinguishable oleophobicity sharing a common feature: as the corrosion lasts for a longer time, the substrates demonstrate a stronger oleophobicity, and reach superoleophobicity with a CA close to 170°, as quantitatively plotted in Fig. 5. The corrosion enhances the oleophobicity of the alloy surface. As indicated in Fig. 5, initially, the CA increases dramatically for a short duration of the corrosion, and then shows saturation for a sufficient corrosion time (9 h here). All of the samples with different polishing processes exhibit the same tendency for the CA variation, though the initial roughness of the samples (by various polishing processes) is quite different. Additionally, for the same corrosion time, the sample becomes more oleophobic when its initial roughness is smaller. For instance, the CA increases to 155° for the bare sample and to 163° for the finely polished sample, both of which have been corroded for 5 h (the fourth ellipse in Fig. 5). Another phenomenon found is that CAs on different substrates just after polishing but without corrosion depict the opposite tendency to those on corroded substrates (indicated by the downward arrow in Fig. 5).

4 Discussion

4.1 Roughness versus corrosion

The corrosion behavior has been extensively studied on various metallic alloys, and it is widely accepted that there

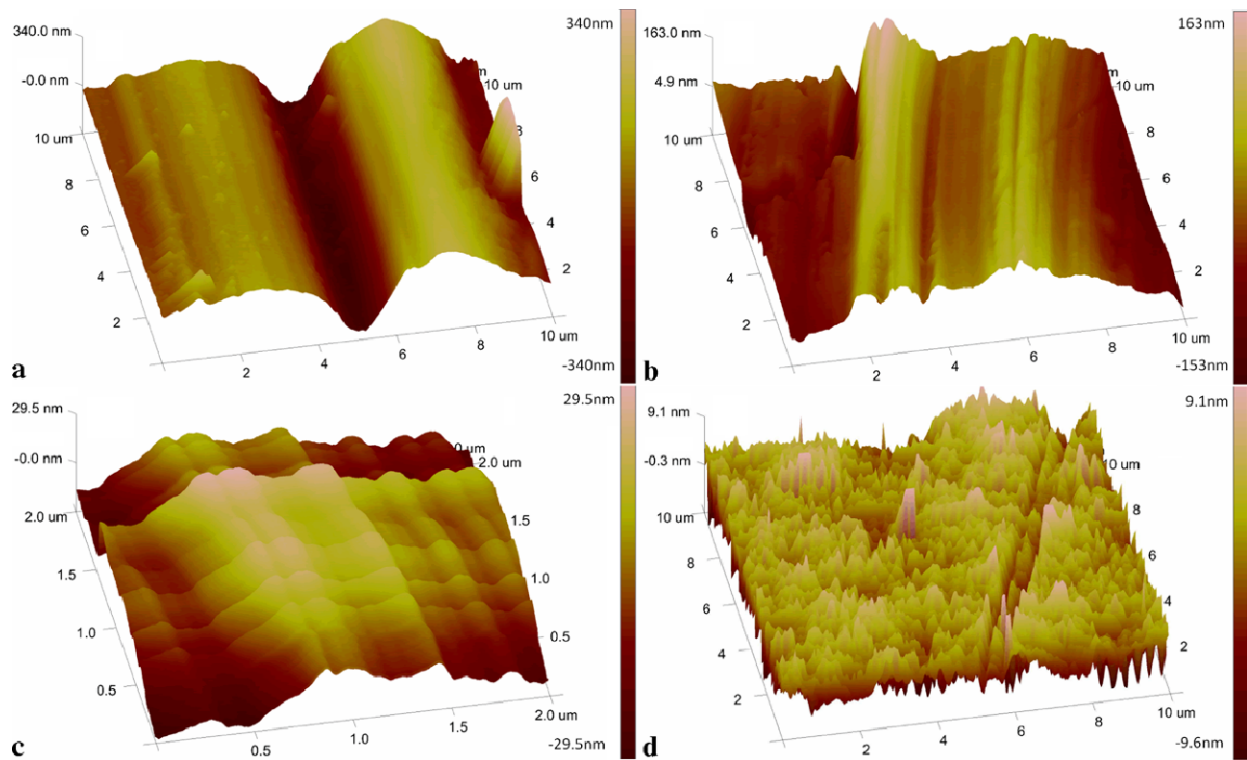


Fig. 2 AFM images for surface morphology of different alloy substrates. (a) Bare sample, (b) preliminarily polished sample, (c) further polished sample, (d) finely polished sample

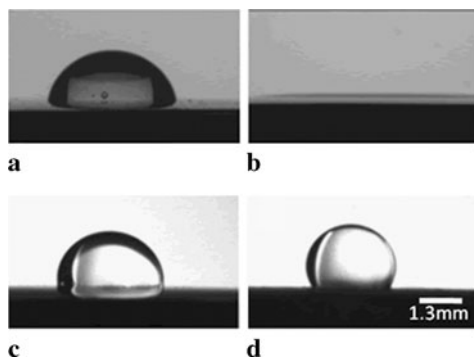


Fig. 3 Snapshots of water and oil droplets on different substrates in air and in water. Water droplet (a) and oil droplet (b) on finely polished substrates in air. Oil droplets in water lying on finely polished substrate (c) and bare substrate (d) with corresponding CAs of 85°, 122°, respectively. The scale bar is 1.3 mm for all the snapshots

are mainly three kinds of microscopic corrosion regimes, i.e., “pitting corrosion,” “intergranular corrosion,” and “general corrosion” [32–34], which are dominant in different intervals throughout the corrosion process. In this study, the finely polished sample is employed to investigate the relationship between the surface roughness and corrosion time, and the result is shown in Fig. 6.

Figure 6 shows that the surface roughness has a strong dependence on the corrosion time, and that the surface rough-

ness exhibits a quick increase within just several minutes at the beginning and then reaches the maximum about 30 min later. The results suggest that “pitting corrosion” is dominant in the very early stage. During this stage, pits form immediately as the sample is immersed into the HCl solution, and simultaneously the depth of the pits greatly increases, thus increasing the roughness. At the same time, “intergranular corrosion” can wear away the areas near the pits, creating peaks and valleys, which also contributes to the increase of the surface roughness. About 30 min later, the surface roughness begins to decrease gradually, which could be interpreted by saying that “general corrosion” becomes dominant from then on. During this stage, the peaks and the valleys are depressed, resulting in a decrease of the surface roughness when the corroding continues. This general tendency is consistent with the reports on metallic alloys utilizing various techniques [35–38]. Thus it is safe to classify the general regimes for the corrosion of the alloy in the present work: sharpening of the roughness at the early stage, followed by maximum amplification of the roughness, and finally smoothing to saturation. We note here that the main focus in this report is on the tendency of the alloy surface roughness under corrosion conditions, plus the complexity of the corrosion mechanism. The effect of corrosion on the alloy surface roughness is not fully investigated here, but is a topic of interest for our following studies.

Fig. 4 Micrographs of oil droplets on samples corroded for different times. Columns (a), (b), (c), and (d) represent the CA increase for the bare, preliminarily polished, further polished, and finely polished samples, respectively. The scale bar is 1.3 mm for all the micrographs

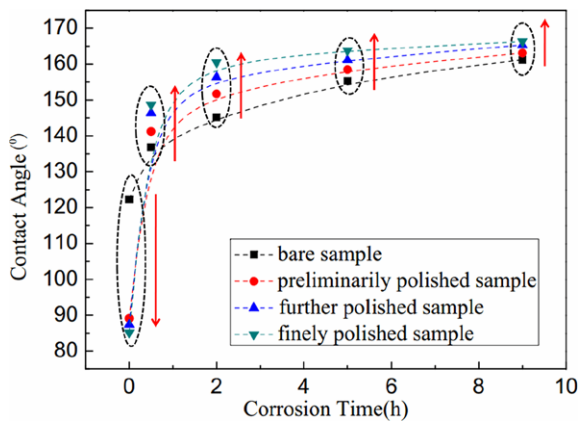
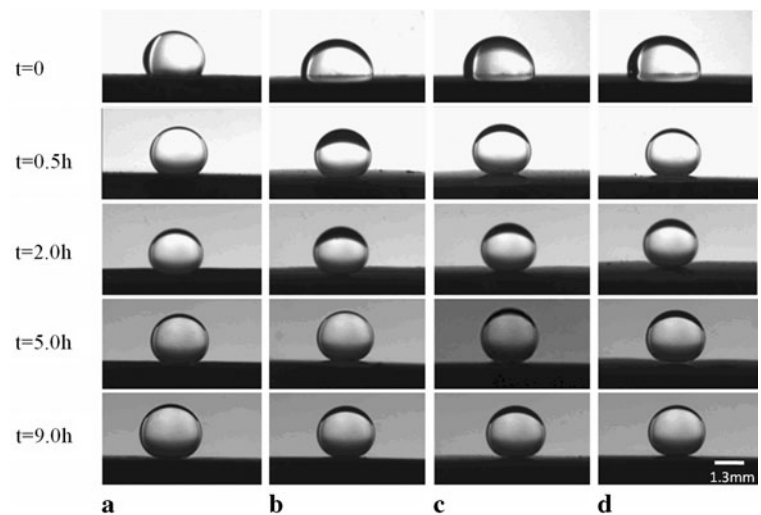


Fig. 5 CA dependence on the corrosion time for oil drops on different substrates with various initial roughnesses. The dashed lines are drawn as guides to the eye

4.2 Effect of naturally obtained high-energy inorganic coating on the wetting transition

Note in Fig. 5 that there is a sharp wetting transition from oleophilic state to oleophobic state between the corrosion intervals from 0 h to 0.5 h for different types of samples. Most of the methods employed to realize the transition concern the aids of external pressure, vibration of the droplet, coating, and so forth. We assume here that a stable, high-energy, inorganic coating layer was obtained, and this has motivated us to perform XRD and XPS examinations on the surfaces of the corroded samples (see Fig. 7).

Evidence can be concluded from Fig. 7a and 7b that an inorganic film of Fe_2O_3 was obtained on the surface of the two types of samples, since the binding energy of Fe2p in Fe_2O_3 is about 710.8 eV [39], which is consistent with the detected XPS result here. While the XRD instrument has a strong penetration capability and only the iron element was detected, as Fig. 7c depicts, this could be due to the thick-

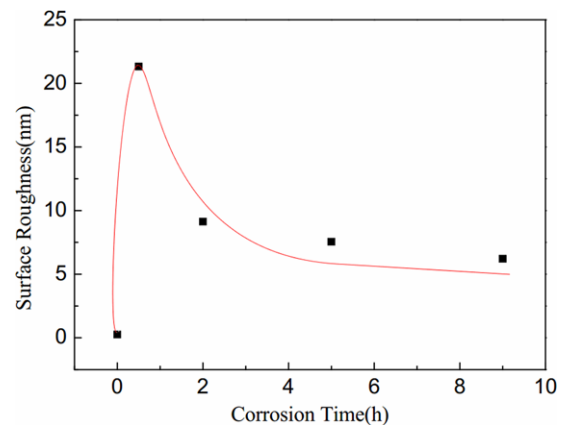


Fig. 6 The dependence of surface roughness (RMS values) on corrosion time for finely polished sample measured by AFM. The solid line is an eye-guide line to show the basic tendency of surface roughness

ness of the coating layer of Fe_2O_3 , which is especially small. The coating layer of Fe_2O_3 has a high surface tension of 1.357 mN/m^{-1} (at room temperature) [40], which could account for the sharp wetting transition from oleophilic state to oleophobic state in our report. We note that the increase of roughness induced by corrosion may affect the wetting property to some extent within this period, but the occurrence of the Fe_2O_3 coating layer with a high surface tension will dominantly control the wetting state from an energy point of view. Considering the formation of the Fe_2O_3 coating layer, we assume there are two possibilities. One is the cleaning process for the corroded samples to remove the residues of corrosion products. During this process oxygen will inevitably contact the corroded samples' surface plus the surface of the alloy that has just been corroded and is active, leading to the easy oxidation of iron and thus forming the high-energy Fe_2O_3 coating layer. The other possibility concerns the CA measurement of the oil droplet under Di-water, in which the sample surface will react with dissolved

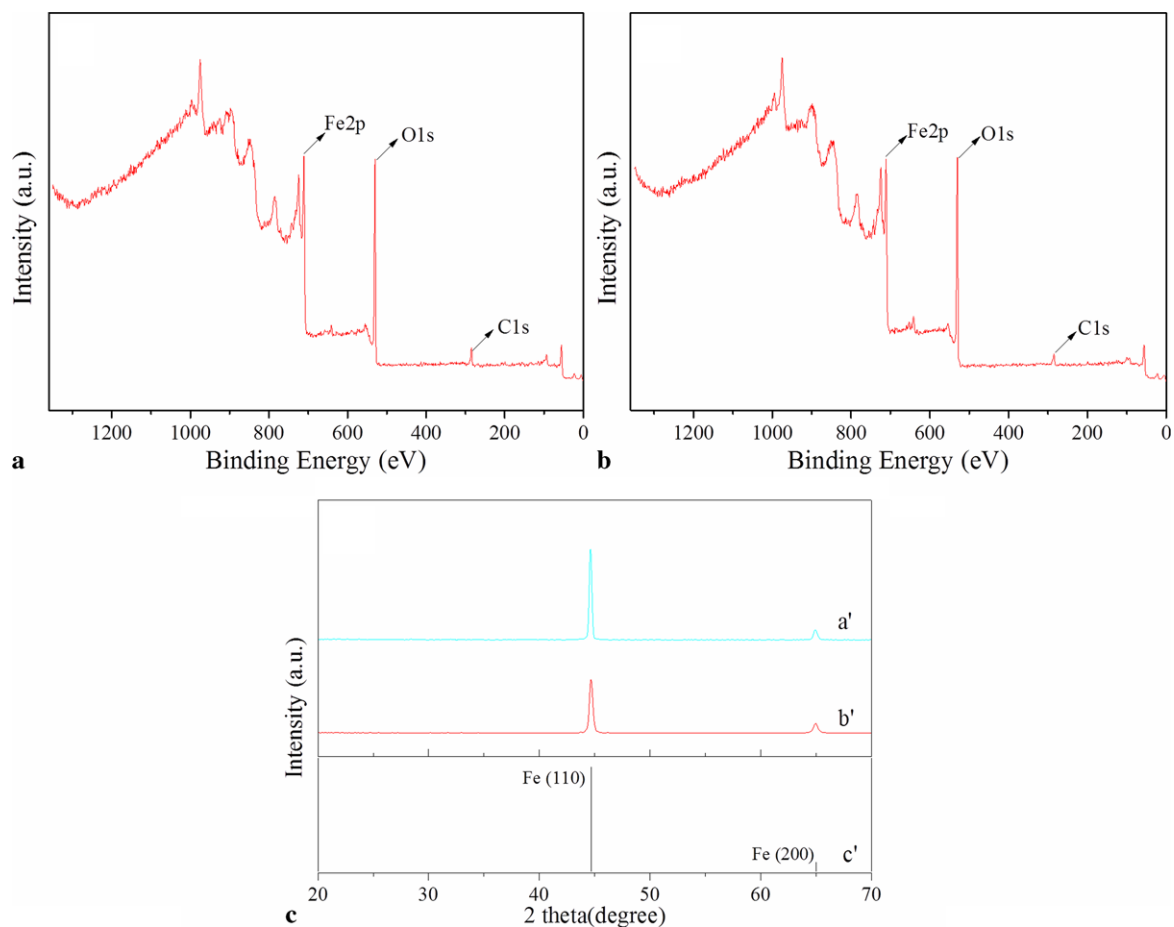


Fig. 7 XPS survey spectra of (a) polished sample and (b) preliminarily polished sample, and (c) XRD patterns of the two types of samples in which a', b', c' represent the polished sample, preliminarily polished

sample, and standard pattern of iron, respectively. Both of the samples have been corroded for 9 h

oxygen. Although the Di-water has been boiled, the possibility should be considered.

4.3 Effect of surface roughness on wettability

The CA of an oil droplet on a smooth solid surface under water can be written as [41]

$$\cos \theta_{ow} = \frac{\gamma_{ov} \cos \theta_o - \gamma_{vw} \cos \theta_w}{\gamma_{ow}} \quad (1)$$

where γ_{ov} , θ_o and γ_{vw} , θ_w are the surface energy and equilibrium CA of oil and water droplets in air, respectively; γ_{ow} and θ_{ow} are the oil–water interfacial energy and the CA of an oil droplet on a smooth solid surface in water, respectively.

For the experimental CA measurements in air, the CAs of oil (θ_o) and water (θ_w) droplets on a finely polished surface are $\sim 0^\circ$ and $\sim 72^\circ$, respectively. Taking the values $\gamma_{ov} = 24.15 \text{ mNm}^{-1}$ [42], $\gamma_{vw} = 73 \text{ mNm}^{-1}$ (as the oil 1,2-dichloroethane is slightly miscible in water, the actual value of γ_{vw} is a little smaller than 73 mNm^{-1}), and

$\gamma_{ow} = 28.1 \text{ mNm}^{-1}$ [43], Eq. (1) gives $\cos \theta_{ow} = 0.076$; thus $\theta_{ow} = 85^\circ$, which agrees well with the measured CA ($\sim 85^\circ$, Fig. 3c) in the present work. These results indicate that Eq. (1) successfully predicts the CA for an oil droplet resting on a smooth surface in a water environment. However, whether it is a good prediction for the case of the rough surface or not should be considered as follows.

The consideration of the CA of a droplet on a rough solid surface composed of solid and trapped air, for which the size of the roughness details is much smaller than the size of the droplet, could be referred to the Wenzel [9] and Cassie and Baxter [10] models. In Wenzel's approach, the liquid is assumed to fill up the rough surface in the water–air–solid system, which is considered in the oil–water–solid system here; thus the apparent CA can be expressed as

$$\cos \theta_{wen} = r \cos \theta_{ow} \quad (2)$$

where r is the roughness factor defined here as the ratio of the actual solid–oil contact area to the projected area on the horizontal plane. In Cassie and Baxter's approach, it is

assumed that the droplet will settle on the peaks of roughness geometry; i.e., in the oil–water–solid system here, the oil droplet does not fill the grooves on the rough surface (Fig. 1b). In this regard, the CA of the oil droplet can be written as

$$\cos \theta_{oc} = f \cos \theta_{ow} + f - 1 \tag{3}$$

where f is the area fraction of the solid–oil interface, and θ_{oc} is the apparent CA of the oil droplet on the rough surface in water.

Extensive studies have been performed to investigate the validity of the Wenzel and Cassie–Baxter models to predict wetting properties and the transition between them under various conditions [44–49]. In particular, considering the Wenzel model, the roughness factor $r > 1$; thus, following its prediction, $\theta_{wen} > \theta_{ow} > 90^\circ$ for a hydrophobic surface, while for a hydrophilic surface $\theta_{wen} < \theta_{ow} < 90^\circ$. Therefore, roughness enhances both hydrophobicity and hydrophilicity. However, in this report, θ_{ow} is 85° (Fig. 2c), and thus the CA of the oil droplet on the corroded surfaces cannot be larger than 85° if it is in Wenzel’s regime. Nevertheless, all of the CAs of the oil droplets on the corroded surfaces are much larger than 85° as depicted in Fig. 5, indicating that Wenzel’s theory is not applicable here. Thus, the Cassie–Baxter theory is reasonable for predicting the CA variations, and we will further examine the validity of the theory by employing a classical roughness geometrical structure as follows.

To understand the CA in the present experiments, based on the Cassie–Baxter equation, we approximately consider the rough surface to be made of periodically distributed square pillars (side view of Fig. 8a). The periodic structure is made from solid pillars $a/2 \times a/2$ in size and b apart from each other (Fig. 8b). Additionally, for comparison, a simpler consideration for this periodic structure is also given in one dimension (Fig. 8c). Similarly, some literatures represented an analogous approximation for the theoretical analysis of the lotus effect [50–52], which offers insightful guidance for the fabrication of artificially superhydrophobic surfaces. Based on the assumptions above, we can derive the area fractions in the models of one and two dimensions as $f_1 = 1/(2b/a + 1)$ (Fig. 8c) and $f_2 = 1/(b/a + 1)^2$ (Fig. 8b), respectively.

For the case of a rough surface, a bare sample (without polishing) (Fig. 2a) is taken first as an example for the estimation of the values a and b (defined in Fig. 8). The surface morphology is imaged by AFM (Fig. 9a), and the cross section is plotted in Fig. 9b for a selected box marked in Fig. 9a. In order to estimate the values a and b , the peaks (pillar) and the adjacent valley are employed, respectively, and this is used as the general method for all of the following cases. It is at the position of approximately 80 % of the pillar height (the distance from the lowest point to

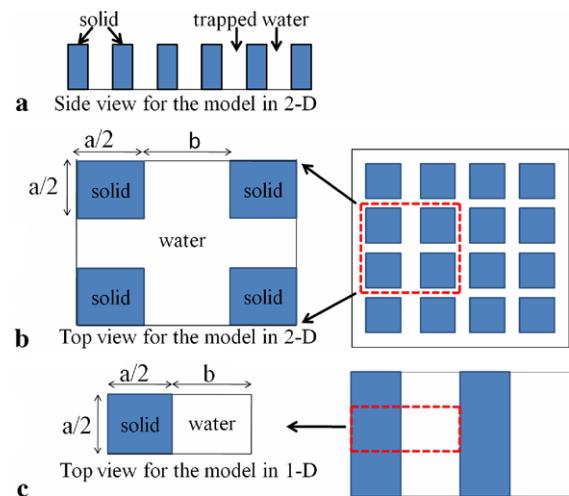


Fig. 8 Sketch of rough surface geometry of periodic pillars in two dimensions for side view (a) and top view (b), and in one dimension for top view (c)

the highest point) that the widths a_1, a_2 of the two adjacent pillars are taken, and the distance between these two adjacent pillars is taken as the value of b (Fig. 9b). The substrate surface can be considered to consist of innumerable units of the square shown in Fig. 8b and 8c. Under the condition of the simplified consideration above, from the AFM images (Fig. 9), the sizes of $a_1/2 = 1.576 \mu\text{m}$, $a_2/2 = 2.308 \mu\text{m}$ are estimated, which gives an average value of $a = (a_1 + a_2)/2 = 3.884 \mu\text{m}$. Taking the estimation of $b = 2.353 \mu\text{m}$, we have $f_1 = 0.393$ (1-D model) and $f_2 = 0.318$ (2-D model), and thus we calculate that $\theta_{oc1} = 125^\circ$ (1-D model) and $\theta_{oc2} = 131^\circ$ (2-D model) according to Eq. (3). Those values agree nicely with the CA measurement ($\theta_{oc} \sim 122^\circ$), implying that the assumption of water penetrating into the trenches on the substrate surface in the Cassie–Baxter regime is reasonable to adopt to predict the apparent CA for the oil drop on a rough substrate under water here. It is worthwhile to note that the estimation of the area fraction of f pertaining to Fig. 8 has to been considered for a certain region, and this approximation is reasonable since the surface of the sample has a similar morphology everywhere (this has been checked by several AFM measurements; the data is not shown here).

To explain the phenomenon of the increase of the surface oleophobicity over corrosion time, a simplified mechanism is proposed, as shown in Fig. 10.

It is reasonable that the surface height decreases with longer corrosion time due to the effect of “general corrosion” discussed in Sect. 4.1, which has been checked by the AFM measurements for all the samples with different corrosion time, and is consistent with the results reported by Alvarez et al. [38]. In our simplified model (Fig. 10), the dimensions of a and b are defined in the same way as in Fig. 9; a_0 and b_0 are the initial values of the peak and valley,

Fig. 9 AFM images for the bare sample before corrosion. (a) Topographic image and (b) cross section averaged for the area marked by the rectangular box in (a)

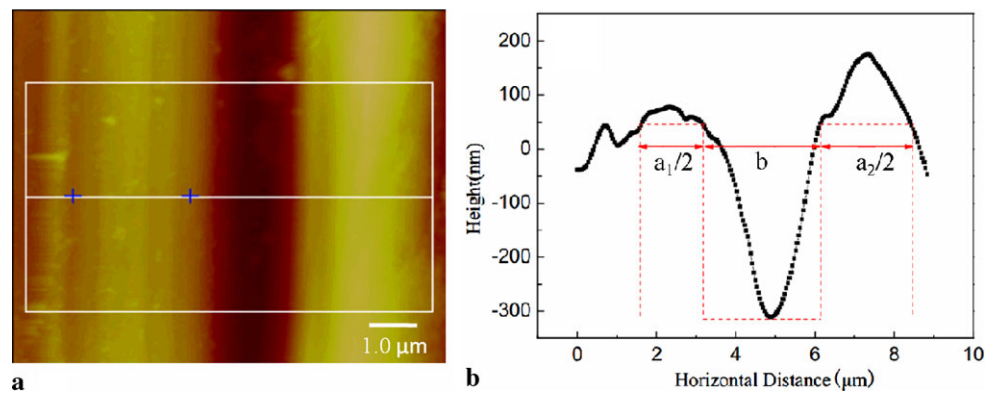
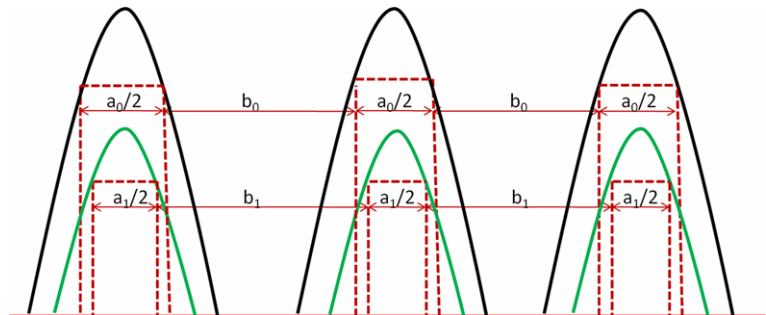


Fig. 10 Illustration of the corrosion evolution of the substrate surface. Black and green curves represent the morphology of the surface before and after corrosion, respectively. a_0 and b_0 are the initial values of the peak and valley; a_1 and b_1 are the values after the corrosion for a certain time



and a_1 and b_1 are the values after the corrosion for a certain time. As shown in Fig. 4, the CA measurement is carried out again in the water environment. According to Eq. (3), it is expected that the apparent CA θ_{oc} increases as the area fraction f decreases. To demonstrate the connection between the corrosion and the wettability, and validate the prediction of Eq. (3) for a corroded surface, two samples with different initial roughnesses of the surface are introduced. The surface morphologies of the two samples that have been corroded for 9 h are examined by AFM as displayed in Fig. 11. We also performed a SEM examination in order to obtain the overall surface morphologies of the two corroded samples; the results are shown in Fig. 12.

Figures 12b and d show the microscopic surface morphology of the two types of sample that have been corroded for 9 h, which offers strong evidence that our simplified corrosion mechanism as displayed in Fig. 10 is reasonable, and furthermore demonstrates that the CA calculating method based on the roughness geometrical structure (Fig. 8) and Cassie–Baxter model is valid. In terms of the estimation of the values defined in the Cassie–Baxter model equation (3), we can refer to Fig. 11.

In Fig. 11b, $a = (a_1 + a_2)/2 = 1.503 \mu\text{m}$, $b = 4.600 \mu\text{m}$ for the rougher sample (Fig. 11a), and the calculated apparent CA is $\theta_{oc} = 148^\circ \sim 159^\circ$, which is close to the measured apparent CA (163°). For the smoother sample (Fig. 11c), we have $a = (a_1 + a_2)/2 = 1.275 \mu\text{m}$, and $b = 4.618 \mu\text{m}$ (Fig. 11d); thus the calculated apparent CA, $\theta_{oc} = 151^\circ \sim 162^\circ$, is also close to the measured value

(167°). Simplifying the ridges (or valleys for 1-D) and peaks (or pits for 2-D) as periodically distributed pillars is a seemingly simple approximation to employ the Cassie–Baxter model, and amazingly, the calculated values of CA agree surprisingly well with the experimental ones. Moreover, we should mention that the calculated values from the 2-D model are closer to the measured results than those from the 1-D model. This may result from the fact that the 2-D model provides a better approximation of the surface morphology compared with the 1-D model in the statistical consideration. Therefore, generally speaking, the 2-D model is reasonably suggested to successfully predict the wetting properties.

5 Conclusions

In summary, a practical new method has been developed to successfully control the wettability of an alloy surface via subtle and simple corrosion. Using this method, the underwater superoleophobicity of the pipeline alloy substrate can be realized at a large scale, reproducibly, without requiring a complicated micro/nano manufacturing process or sophisticated chemical coatings. The naturally obtained, stable, high-energy inorganic coating layer of Fe_2O_3 makes the sharp transition from the oleophilic state to the oleophobic state possible. Along with this, the controllable corrosion

Fig. 11 AFM micrographs of different samples corroded for 9 h. (a) Topographic image and (b) cross section of region in (a) for the rougher (preliminarily polished) sample; (c) topographic image and (d) cross section of region in (c) for the smoother (polished) sample

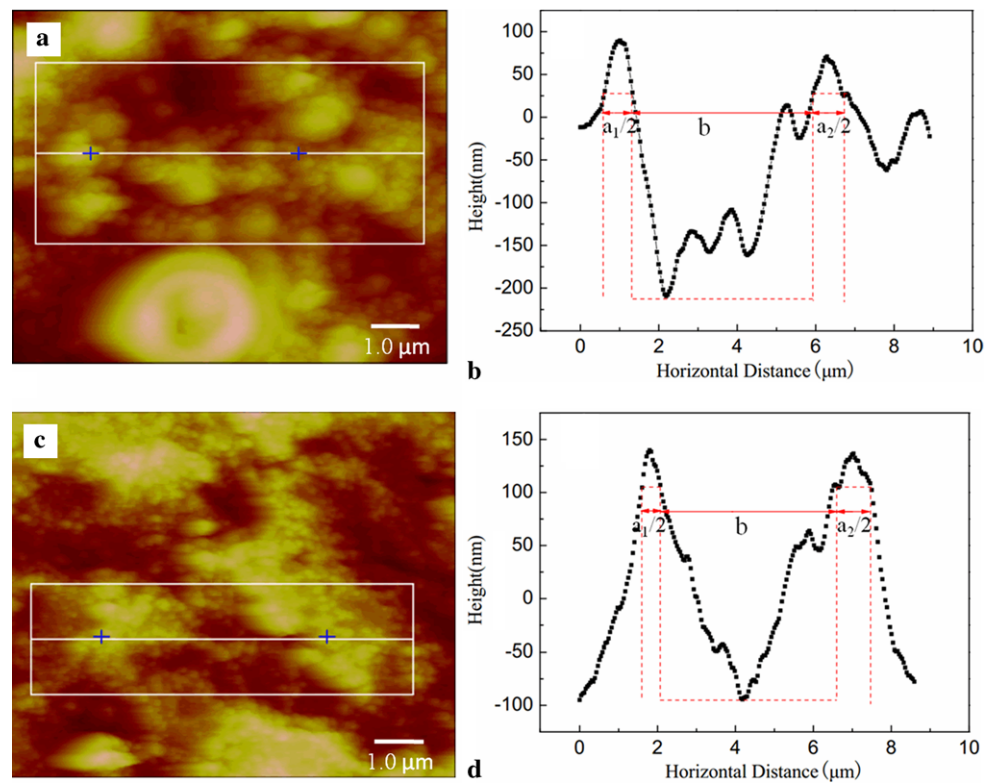
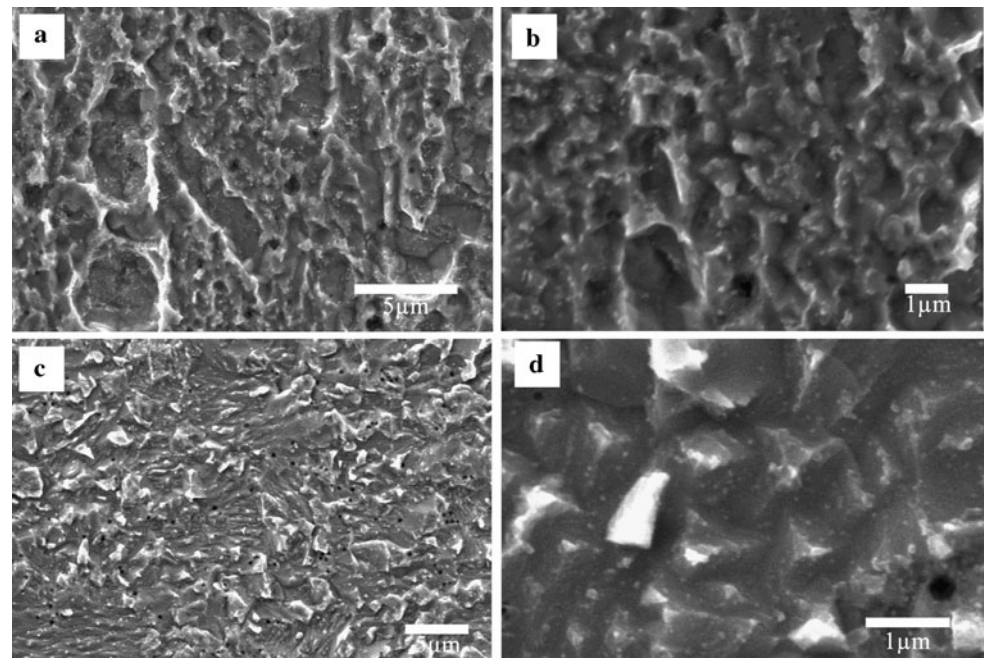


Fig. 12 SEM images of (a) rougher (preliminarily polished) sample and (c) smoother (polished) sample. (b) and (d) are zoom-in views of parts (a) and (c), respectively. Both of the samples have been corroded for 9 h



contributes to the decrease of f , which is the area fraction of solid-oil interface in our system as indicated in Cassie–Baxter theory, consequently leading to a significant increase of CA to $\sim 170^\circ$ for the oil drop resting on the substrate in a water environment. Moreover, the analytical methods proposed here based on the roughness geometrical structure and Cassie–Baxter theory successfully explain the oleophobicity

variations and precisely predict the measured apparent CA. We note that the corrosion behavior has always been complicated and that the various mechanisms of the corrosion dynamics are not fully investigated here. The interesting correlations among the surface roughness, corrosion, and the wettability are still open to more exploration for future study. In the present work, our protocol will be instructive for the

practical water/oil separation process and drag reduction applications in the oil industry.

Acknowledgements The authors gratefully acknowledge the support by NSFC (No. 11104218), the Natural Science Basic Research Plan in Shaanxi Province of China (Program No. 2010JZ001), and the Scientific Research Foundation for Returned Overseas Chinese Scholars (Shaanxi Administration of Foreign Expert Affairs, 2011).

References

1. K. Hay, M. Dragila, J. Liburdy, J. Colloid Interface Sci. **325**, 472 (2008)
2. J.W. Cahn, J. Chem. Phys. **66**, 3667 (1977)
3. C. Ebner, W. Saam, Phys. Rev. Lett. **38**, 1486 (1977)
4. X. Feng, J. Zhai, L. Jiang, Angew. Chem. **44**, 5115 (2005)
5. W.L. Min, B. Jiang, P. Jiang, Adv. Mater. **20**, 3914 (2008)
6. T. Kako, A. Nakajima, H. Irie, Z. Kato, K. Uematsu, T. Watanabe, K. Hashimoto, J. Mater. Sci. **39**, 547 (2004)
7. A. Chunder, K. Etcheverry, G. Londe, H.J. Cho, L. Zhai, Colloids Surf. A, Physicochem. Eng. Asp. **333**, 187 (2009)
8. C. Lee, C.-H. Choi, C.-J.C. Kim, Phys. Rev. Lett. **101**, 64501 (2008)
9. R.N. Wenzel, J. Phys. Chem. **53**, 1466 (1949)
10. A. Cassie, S. Baxter, Trans. Faraday Soc. **40**, 546 (1944)
11. A. Tuteja, W. Choi, M. Ma, J.M. Mabry, S.A. Mazzella, G.C. Rutledge, G.H. McKinley, R.E. Cohen, Science **318**, 1618 (2007)
12. B. Bhushan, Y.C. Jung, Prog. Mater. Sci. **56**, 1 (2011)
13. C. Borgs, J. De Coninck, R. Kotecký, M. Zinque, Phys. Rev. Lett. **74**, 2292 (1995)
14. K.H. Chu, R. Xiao, E.N. Wang, Nat. Mater. **9**, 413 (2010)
15. L. Zhai, F.C. Cebeci, R.E. Cohen, M.F. Rubner, Nano Lett. **4**, 1349 (2004)
16. X. Feng, L. Feng, M. Jin, J. Zhai, L. Jiang, D. Zhu, J. Am. Chem. Soc. **126**, 62 (2004)
17. K.K.S. Lau, J. Bico, K.B.K. Teo, M. Chhowalla, G.A.J. Amaratunga, W.I. Milne, G.H. McKinley, K.K. Gleason, Nano Lett. **3**, 1701 (2003)
18. D. Wang, X. Wang, X. Liu, F. Zhou, J. Phys. Chem. C **114**, 9938 (2010)
19. V. Zorba, E. Stratakis, M. Barberoglou, E. Spanakis, P. Tzanetakis, S.H. Anastasiadis, C. Fotakis, Adv. Mater. **20**, 4049 (2008)
20. E.K. Her, T.J. Ko, K.R. Lee, K.H. Oh, M.W. Moon, Nanoscale **4**, 2900 (2012)
21. W. Choi, A. Tuteja, S. Chhatre, J.M. Mabry, R.E. Cohen, G.H. McKinley, Adv. Mater. **21**, 2190 (2009)
22. L. Joly, T. Biben, Soft Matter **5**, 2549 (2009)
23. J. Zhang, S. Seeger, Angew. Chem. Int. Ed. **50**, 6652 (2011)
24. L. Gao, T.J. McCarthy, J. Am. Chem. Soc. **128**, 9052 (2006)
25. W. Tang, Y. Huang, W. Meng, F.-L. Qing, Eur. Polym. J. **46**, 506 (2010)
26. Z. Xue, S. Wang, L. Lin, L. Chen, M. Liu, L. Feng, L. Jiang, Adv. Mater. **23**, 4270 (2011)
27. M. Liu, S. Wang, Z. Wei, Y. Song, L. Jiang, Adv. Mater. **21**, 665 (2009)
28. X. Liu, J. Zhou, Z. Xue, J. Gao, J. Meng, S. Wang, L. Jiang, Adv. Mater. **24**, 3401 (2012)
29. L. Cao, T.P. Price, M. Weiss, D. Gao, Langmuir **24**, 1640 (2008)
30. Y.C. Jung, B. Bhushan, Langmuir **25**, 14165 (2009)
31. B. Balu, V. Breedveld, D.W. Hess, Langmuir **24**, 4785 (2008)
32. G. Makar, J. Kruger, Int. Mater. Rev. **38**, 138 (1993)
33. A. Di Schino, J. Kenny, J. Mater. Sci. Lett. **21**, 1631 (2002)
34. P. Marcus, *Corrosion mechanisms in theory and practice*, 2nd edn. (Dekker, New York, 2002)
35. G. Song, A. Atrens, Adv. Eng. Mater. **5**, 837 (2003)
36. E.S.M. Sherif, J. Potgieter, J. Comins, L. Cornish, P. Olubambi, C. Machio, Corros. Sci. **51**, 1364 (2009)
37. C.M. Sulyma, D. Roy, Corros. Sci. **52**, 3086 (2010)
38. R.B. Alvarez, H.J. Martin, M. Horstemeyer, M.Q. Chandler, N. Williams, P.T. Wang, A. Ruiz, Corros. Sci. **52**, 1635 (2010)
39. J.F. Moulder, W.F. Stickle, P.E. Sobol, D. Bombem, *Handbook of X-ray photoelectron spectroscopy* (Perkin-Elmer Co., Eden Prairie, 1992)
40. E.M. Petrie, *Handbook of Adhesives and Sealants* (McGraw-Hill, New York, 2000)
41. M. Järn, B. Granqvist, J. Lindfors, T. Kallio, J. Rosenholm, Adv. Colloid Interface Sci. **123**, 137 (2006)
42. D.R. Lide, *CRC handbook of chemistry and physics*, 90th edn. (CRC Press, Boca Raton, 2009)
43. A. Popov, T. Borisova, J. Colloid Interface Sci. **236**, 20 (2001)
44. T. Koishi, K. Yasuoka, S. Fujikawa, T. Ebisuzaki, X.C. Zeng, Proc. Natl. Acad. Sci. USA **106**, 8435 (2009)
45. H.Y. Erbil, C.E. Cansoy, Langmuir **25**, 14135 (2009)
46. N.A. Patankar, Langmuir **20**, 7097 (2004)
47. C. Ishino, K. Okumura, D. Quéré, Europhys. Lett. **68**, 419 (2007)
48. D. Bonn, D. Ross, Rep. Prog. Phys. **64**, 1085 (2001)
49. A. Marmur, Langmuir **20**, 3517 (2004)
50. N.A. Patankar, Langmuir **20**, 8209 (2004)
51. N.A. Patankar, Langmuir **19**, 1249 (2003)
52. Y. Kwon, N. Patankar, J. Choi, J. Lee, Langmuir **25**, 6129 (2009)